Simplified modeling of self-piercing riveted joints for crash simulation with a modified version of *CONSTRAINED_INTERPOLATION_SPOTWELD

Matthias Bier, Silke Sommer

Fraunhofer Institute for Mechanics of Materials IWM, Germany

1   Abstract

The requirements for energy efficiency and lightweight construction in automotive engineering rise steadily. Therefore a maximum flexibility of the used materials is necessary and new joining techniques are constantly developed. The resulting large number of joints with different properties leads to the need to provide for each type of joint an appropriate modeling method for crash simulation.

In this paper an approach for a simplified model of a self-piercing riveted joint for crash simulation will be discussed. The used simplified model is a modified version of the *CONSTRAINED_ INTERPOLATION_SPOTWELD. Firstly the realized modifications as a changed yield and failure behavior will be explained and illustrated. Therefore simulation results of the default and the modified version of the *CONSTRAINED_INTERPOLATION_SPOTWELD will be compared. Secondly the procedure to identify the appropriate model parameters will be presented and shown in an exemplary manner. At once the advantages and limitations of the model will be demonstrated. At least the quality of the model will be validated using simulations of different loaded T-joint experiments, which represents the connection between the rocker panel and the B-pillar. For this purpose three different characteristics will be taken into account: the global responses like the calculated and measured force vs. displacement curve of the punch, the local failure behavior and the order of failure of the rivet joints, and at last the internal forces in the simplified model.

2   Introduction

In this paper self-piercing riveting, more precisely self-piercing riveting with a semi-tubular rivet, is examined. Self-piercing riveting (SPR) belongs to the group of mechanical joining techniques to join two or more sheets.The process can be divided into four different steps as described by He et al. [1] (see Fig. 1). The first step is the clamping. Thereby the blank holder and the die press the assembly parts, which will be joined. Thus the relative position of the two or more sheets is fixed. Also the rivet is put on the sheets. The second step is the piercing. This is the first stage of the process, where deformations occur. The punch drives the rivet through the top sheet metal into the bottom sheet metal. In doing so the rivet punches a hole in the top sheet and the punched-out top sheet material flows inside the rivet. The third step is the flaring. The die in combination with the material inside the rivet deforms the rivet, thus an interlock is formed. The last step is the releasing. In this step, the punch stops pushing the rivet and the blank holder releases the joined sheets. The riveting process is finished.

The advantage of SPR is the possibility to join a range of dissimilar material combinations. The only requirement to the joined materials is an appropriate ductility, so that the joint can be formed appropriately. Furthermore the joining process of self-piercing rivets doesn't affect the microstructure and thus the properties of the joined materials, as it can be observed in thermal joining processes. These advantages are the reasons, why SPR is increasingly used in lightweight construction of automotive engineering, especially in case of joints between two sheets of aluminum or aluminum and steel.
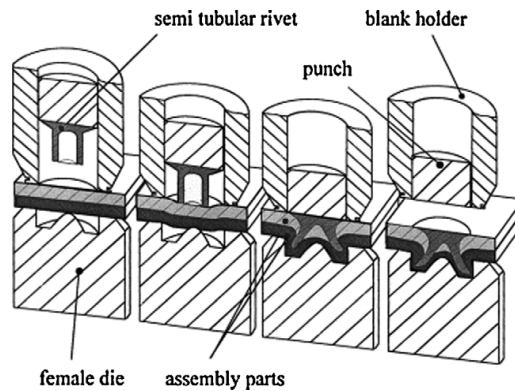
Fig. 1: Joining process of a self-piercing rivet connection, schematic representation [1]

Currently in full vehicle simulations different simplified models are used for punctiform joints. Seeger et al. [2] presented a new failure criterion for a model based on von Mises plasticity. This is known in LS-Dyna as *MAT_100_DA and is now frequently used as a model for spot welds in full vehicle simulations. Bier et al. [3] compared the *MAT_100_DA with the *MAT_COHESIVE_MIXED_MODE_ ELASTOPLASTIC_RATE (*MAT_240), developed by Marzi et al. [4] for adhesively bonded joints, with respect to the usage of spot weld modeling and mesh sensitivity. Hanssen et al. [5] developed a model for self-piercing rivet connections, which is implemented in LS-Dyna as *Constrained_SPR2. The *Constrained_SPR2 considers the relative motion of the connected sheets and calculates the translated forces and moments form these motions. Another model used for punctiform joints is the *Constrained_SPR3 [6], also named *Constrained_Interpolation_Spotweld, which is based on the *Constrained_SPR2 with a different flow and damage behavior. Sommer et al. [7] investigated all these models and in addition the *MAT_169 [6] with respect to modeling possibilities of self-piercing rivet connections. They identified in all models different weaknesses. Hence, the objective of this paper is to present a simplified model optimized in terms of application to self-piercing riveted connections.

3   Description of the SPR models

Both considered models, *Constrained_SPR3 and the modified *Constrained_SPR3, which will be called *CONSTRAINED_SPR3_IWM subsequently, are based on the same procedure to calculate the relative motions. By definition of a reference node N_{ref}, which locates the position of the fastener, and a related radius r of the domain of influence the nodes of the connected sheets are determined, which are used to represent the connection. These nodes can be used to calculate the unit vectors $\vec{n}_m$ and $\vec{n}_s$, which are orthogonal to the master and the slave sheet, respectively. By averaging the normal vectors of both sheets the direction of normal loads is given by

$$\vec{n}_n = \frac{\vec{n}_m + \vec{n}_s}{|\vec{n}_m + \vec{n}_s|} \qquad 3.1$$

and the shear direction is given by

$$\vec{n}_t = (\vec{n}_s \times \vec{n}_m) \times \vec{n}_m \qquad 3.2$$

The total relative displacement $\vec{\delta}$ can be divided into two parts, one part

$$\delta_n = \vec{\delta} \cdot \vec{n}_n \qquad 3.3$$

in direction of $\vec{n}_n$ and the second part

$$\delta_t = \vec{\delta} \cdot \vec{n}_t \qquad 3.4$$

in direction $\vec{n}_t$. This vector of the relative motion can be used to get the translated forces and moments and to describe the flow and failure behavior. At this point the *Constrained_SPR3 and the *Constrained_SPR3_IWM are different:

*Constrained_SPR3
Vector of the relative motion

$$\vec{u} = [\delta_n, \delta_t, \omega_b] \qquad 3.5$$

wherein ω_b is the relative rotation of both sheets.

*Constrained_SPR3_IWM
Vector of the relative motion

$$\vec{u} = [\delta_n, \delta_t] \qquad 3.6$$

In Addition sym, which is an indicator for the symmetry of the rivet load, is calculated by [8]

$$sym = \arccos \frac{\boldsymbol{n}_s \cdot \boldsymbol{n}_m}{|\boldsymbol{n}_s||\boldsymbol{n}_m|} \qquad 3.7$$

Force Calculation

$$\vec{f} = [f_n, f_t, m_b]$$
$$= STIFF \cdot \vec{u}$$
$$= STIFF \cdot [\delta_n, \delta_t, \omega_b] \qquad \text{3.8}$$

Plastic Flow

$$\left[\left(\frac{f_n + \alpha \cdot m_b}{R_n}\right)^{\beta} + \left(\frac{f_s}{R_s}\right)^{\beta}\right]^{\frac{1}{\beta}} - F^0(\bar{u}^{pl}) \le 0 \qquad \text{3.10}$$

Damage/Failure

$$\vec{f}^* = (1-d)\vec{f} \qquad \text{3.12}$$

$$d = \frac{\bar{u}^{pl} - \bar{u}_0^{pl}}{\bar{u}_f^{pl} - \bar{u}_0^{pl}} \qquad \text{3.13}$$

$$\bar{u}_0^{pl} = \bar{u}_0^{pl}(\kappa) \qquad \text{3.14}$$

$$\bar{u}_f^{pl} = \bar{u}_f^{pl}(\kappa) \qquad \text{3.15}$$

$$\kappa = \frac{2}{\pi} \arctan\left(\frac{f_n + \alpha \cdot m_b}{f_s}\right) \qquad \text{3.16}$$

Force Calculation

$$\vec{f} = [f_n, f_t]$$
$$= STIFF \cdot \vec{u}$$
$$= STIFF \cdot [\delta_n, \delta_t] \qquad \text{3.9}$$

Plastic Flow

$$\left[\left(\frac{f_n}{R_n \cdot (1 - \alpha_1 \cdot sym)}\right)^{\beta_1} + \left(\frac{f_s}{R_s}\right)^{\beta_1}\right]^{\frac{1}{\beta_1}} - F^0(\bar{u}^{pl}) = 0 \qquad \text{3.11}$$

Damage/Failure

$$\vec{f}^* = (1-d)\vec{f} \qquad \text{3.17}$$

$$d = \frac{\bar{u}^{pl} - \bar{u}_0^{pl}}{\bar{u}_f^{pl} - \bar{u}_0^{pl}} \qquad \text{3.18}$$

Calculation of $\bar{u}_f^{pl}$ and $\bar{u}_0^{pl}$ considering the load angle φ

$$\varphi = \arctan\left(\frac{f_n}{f_s}\right) \qquad \text{3.19}$$

and the following equations

$$\left[\left(\frac{\bar{u}_0^{pl,n}}{\bar{u}_{0,ref}^{pl,n} \cdot (1 - \alpha_2 * sym)}\right)^{\beta_2} + \left(\frac{\bar{u}_0^{pl,s}}{\bar{u}_{0,ref}^{pl,s}}\right)^{\beta_2}\right]^{\frac{1}{\beta_2}} - 1 = 0 \qquad \text{3.20}$$

$$\bar{u}_0^{pl,n} = \sin(\varphi) \cdot \bar{u}_0^{pl} \qquad \text{3.21}$$

$$\bar{u}_0^{pl,s} = \cos(\varphi) \cdot \bar{u}_0^{pl} \qquad \text{3.22}$$

$$\left[\left(\frac{\bar{u}_f^{pl,n}}{\bar{u}_{f,ref}^{pl,n} \cdot (1 - \alpha_3 * sym)}\right)^{\beta_3} + \left(\frac{\bar{u}_f^{pl,s}}{\bar{u}_{f,ref}^{pl,s}}\right)^{\beta_3}\right]^{\frac{1}{\beta_3}} - 1 = 0 \qquad \text{3.23}$$

$$\bar{u}_f^{pl,n} = \sin(\varphi) \cdot \bar{u}_f^{pl} \qquad \text{3.24}$$

$$\bar{u}_f^{pl,s} = \cos(\varphi) \cdot \bar{u}_f^{pl} \qquad \text{3.25}$$

Two formulation changes were made between the *Constrained_SPR3 and the *Constrained_SPR3_IWM. The first one is the plastic flow behavior and the second one is in the Damage/Failure calculation. For the plastic flow functions (Eq. 3.10 and 3.11) the changes between the *Constrained_SPR3 and the *Constrained_SPR3_IWM are the negligence of bending moment term and the adding of the influence of a state variable called sym. The motivation of this modification was explained by Bier et al. [9]. To show the differences between the sym-variable and a bending-moment based flow function we looked at joints with large plastic deformation. Therefore we have to consider the deformation of both sheets in the simplified model. Assuming that we are in the area for ideal plastic flow of the *Constrained_SPR3 and therefore no hardening occurs, typically the deformations of the sheets are almost constant and not changing any more. Only the relative displacements in tensile and shear direction are rising, the relative rotation is also constant caused by the constant deformation.

If we assume the shear load is zero

$$f_s = 0 \qquad \text{3.26}$$

and ideal plastic flow occurs with

$$F^0(\bar{u}^{pl}) = 1 \qquad \text{3.27}$$

the flow function 3.10 of the *Constrained_SPR3 in the basic version reduces to

$$\frac{f_n + \alpha \cdot m_b}{R_n} - 1 \le 0 \qquad \text{3.28}$$

Fig. 2a) shows the behavior of a connection, loaded in such a manner. The starting point of the ideal plastic deformation is assumed at a high percentage of the bending term$\left(A: \frac{m_b}{R_n} = 0,4\right)$. A relative motion in tensile direction leads to a trial force in tensile direction f_n at the point B'. The subsequent plastic flow, considering the rule, that the force reduction should be orthogonal to the yield surface, leads to a reduction of both the tensile force and the bending moment (point B). These two steps are repeating in every timestep. The consequence is a stepwise reduction of the bending moment and an increasing tensile force as it is shown in Fig. 2b). If we assume large plastic deformations in normal direction the influence of the bending moment is almost zero at the time of damage initiation. That is

why the bending moment can only affect the beginning of yield and not the failure displacement. In contrast the state variable sym is not affected by the plastic flow. Assuming ideal plastic deformations as it is described above sym has the same value at the beginning of yield and at the point of failure. Hence sym can affect both the yield beginning and the failure behavior.
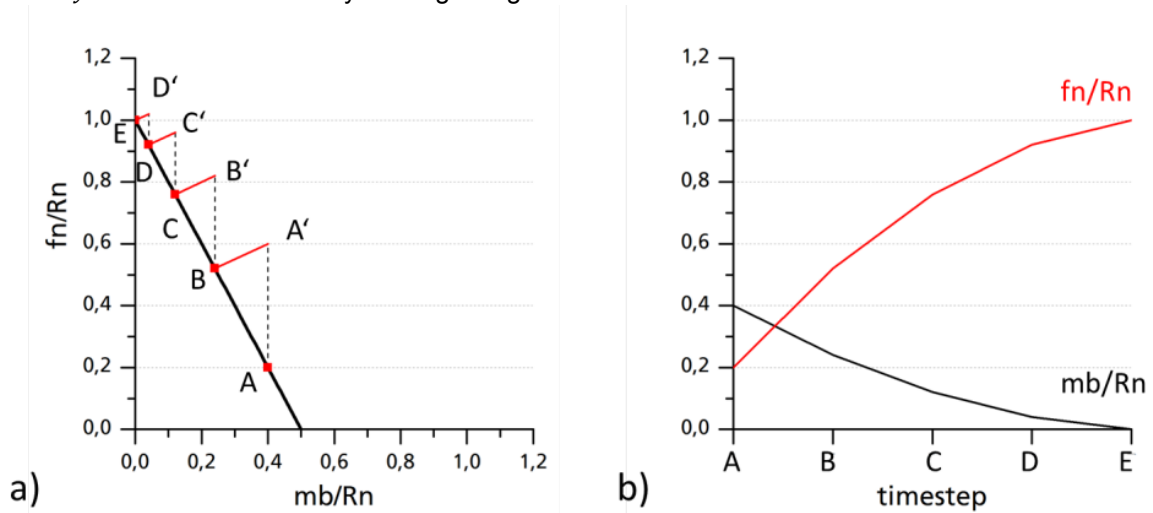

*Fig. 2: a) Stepwise ideal plastic yield behavior of the *Constrained_SPR3 in plane of normal and bending load; b) evolution of normal and bending load in case of ideal plastic yield with large plastic deformations*

The second change is an analytic description of the damage behavior. In the basic version the user can define the plastic effective displacement, when damage initiation and failure occurs, by table data. In the modified version an analytic approach is used to describe the damage and failure behavior. The reason for using an analytic description instead of the tabular definition is a much simpler consideration of rate effects. The rate effects are not considered in this paper, but we take a look here at the differences between the analytic and the tabular definition in case of quasi-static load. The curve progression of $\bar{u}_f^{pl}$ or $\bar{u}_0^{pl}$ is depicted in a schematic manner in Fig. 3 a) for the basic version depending on the load angle $\frac{\pi}{2}\kappa$ and in Fig. 3 b) for the modified version depending on the load angle φ. In case of the tabular definition a piecewise linear dependency can be observed, thereby the number of segments depends on the number of table items. In the case of the analytic approach the shape of the function differs from the table definition and depends on the exponent β_1 or β_2.
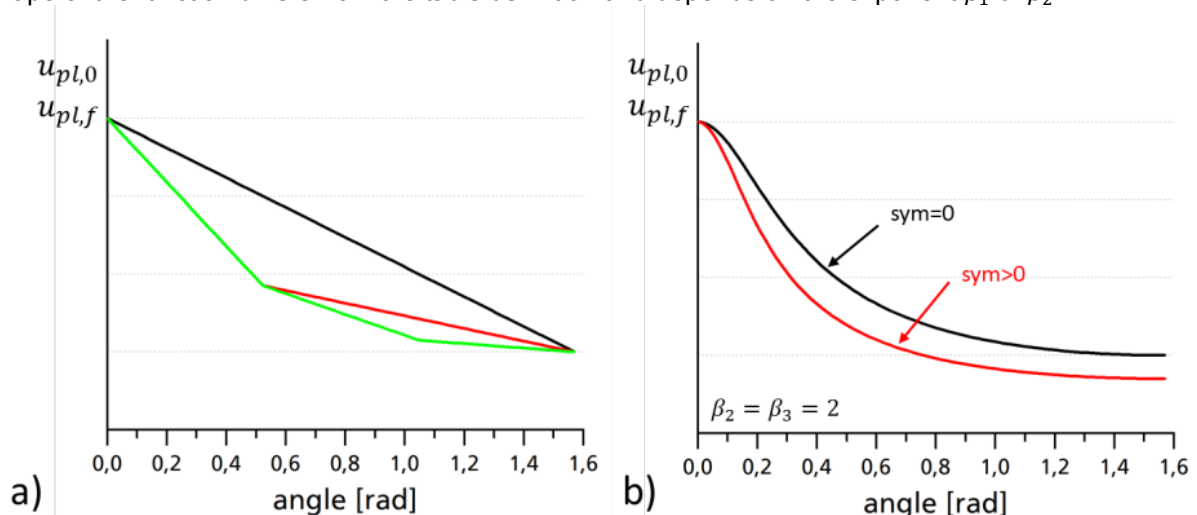

*Fig. 3: Dependency of $\bar{u}_f^{pl}$ or $\bar{u}_0^{pl}$ a) for the *Constrained_SPR3 on the load angle $\frac{\pi}{2}\kappa$ and b) for the modified version *Constrained_SPR3_IWM on the load angle φ*

4   Experimental Database

All experiments, which will be used as a reference for the simulations, were carried out as a part of the AiF-project „Experimentelle Untersuchung und Simulation des Crashverhaltens mechanisch gefügter

Verbindungen", IGF-Vorhaben 352 ZBG, at the Laboratorium für Werkstoff- und Fügetechnik LWF in Paderborn. To characterize the behavior of the self-piercing riveted joints, several tests with the LWF-KS-2 measuring concept (see Fig. 5a)) were made. This concept is defined by specimens, which can be tested under different load angles and loading rates. The specimens consist of two separate u-sections, which are joined together by one punctiform joining technology, which will be characterized. In our case four different load angles are considered, KS-2-0° (pure shear), KS-2-90° (pure tensile), KS-2-30° and KS-2-60° (combination of shear and tensile load). In addition tests with peeling specimens were performed, which are similar to KS-2-90° with one-sided load. The results of these five different experiments are shown in Fig. 4a) and Fig. 5b). If we plot the maximum forces spit ideally in normal and shear fraction in a diagram (Fig. 5c)), which displays the normal force over the shear force, we can interpret the mixed mode behavior of the connection. The result of the peeling specimen can't be added to the diagram, because of the unknown load of the rivet.

For validation T-joint experiments were made (Fig. 4c)). In Fig. 4b) the geometry of the specimen and the load direction (cross the sill) are shown.
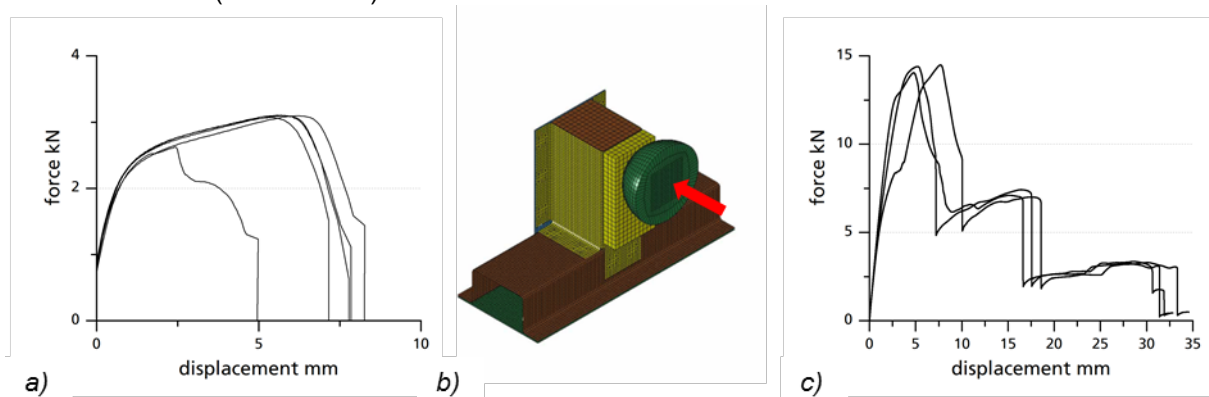

Fig. 4: a) Results of the peeling test; b) geometry of the T-joint test (loading direction – red arrow); c) results of the T-joint test
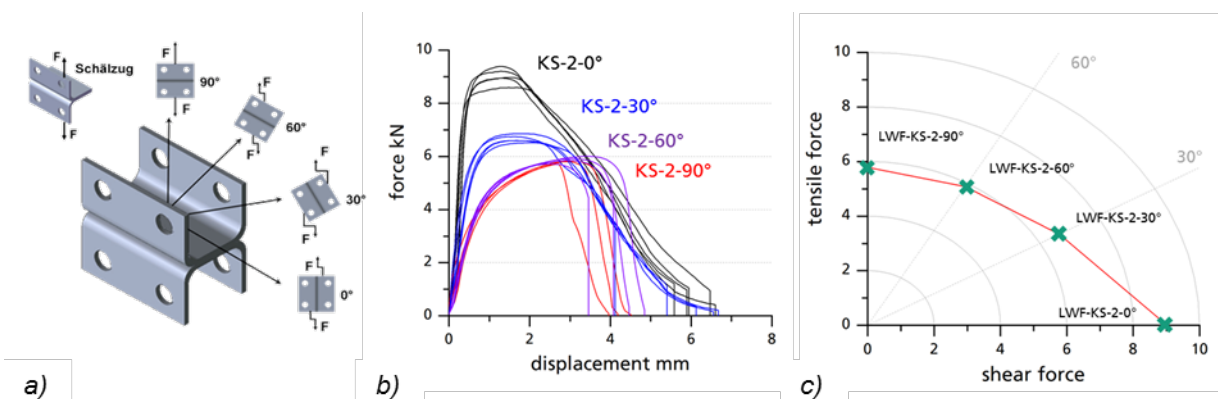

Fig. 5: a) LWF-KS-2 specimen with schematic illustration of the different load angles [9]; b) results of the experiments with KS-2 specimens (0° - black, 30° - blue, 60° - purple, 90° - red); c) diagram of the maximum forces split in shear and normal/tensile fraction

5   Parameter determination/identification

The Parameter identification can be done in the following seven steps.

Step 1:   *Domain of influence*

In the first step the radius of the domain of influence must be defined. Therefore the value should be equal or in the order of the rivet head radius.

Step 2:   *Stiffness*

The Stiffness $STIFF$ of the joint can be determined by the KS-2-0° specimen. Based on the small deformations of the sheets $STIFF$ can be estimated in the linear area by

$$STIFF = \frac{\Delta F}{\Delta s} \ .$$ 5.1

Thereby ΔF and Δs are the force and displacement differences in the approximately linear area, in which the stiffness will be averaged.

Step 3:   *Shape of the flow curve*

Also the flow curve can be determined using the KS-2-0° specimen. As for the determination of the Stiffness, the approach is based on the assumption that the deformations of the sheets are small and only local deformations occur. These small and local deformations can't be described by discretization usually used in crash simulation. So these are all included in the plastic deformations of the simplified model.

$$u_{pl} = \left(s - \frac{F(s)}{STIFF} \right) R_s$$
5.2

Step 4:   *Maximum Forces*

The maximum transferred forces by the *Constrained_SPR3_IWM represented by the parameters R_n and R_s are equal to the maximum measured forces in case of KS-2-90° and KS-2-0° test, respectively.

Step 5:   *Combination of shear and tensile load*

The behavior in case of combined shear and tensile load is determined using the KS-2-30° or -60° test. Also it is possible to use another test with a combined shear and tensile load. Solving the equation

$$\left(\frac{f_n}{R_n} \right)^{\beta_1} + \left(\frac{f_s}{R_s} \right)^{\beta_1} = 1$$
5.3

with the maximum force split in the normal and shear fraction by

$$f_n = sin\varphi \cdot F_{max}^{\varphi}$$
5.4

$$f_s = cos\varphi \cdot F_{max}^{\varphi}$$
5.5

leads to the value of β_1.

Step 6:   *Damage and Failure behavior*

The determination of the parameters for the damage and failure behavior should be done by reverse engineering.

Step 7:   *Influence of sym*

Also the weighting coefficients $\alpha_1, \alpha_2, \alpha_3$ should be determined by reverse engineering by simulation of the peeling test.

The simulation results of the KS-2 specimen with the *Constrained_SPR3_IWM in comparison with test data are shown in Fig. 6. The simulation matches both, the transferred force and failure displacement, in all load cases.
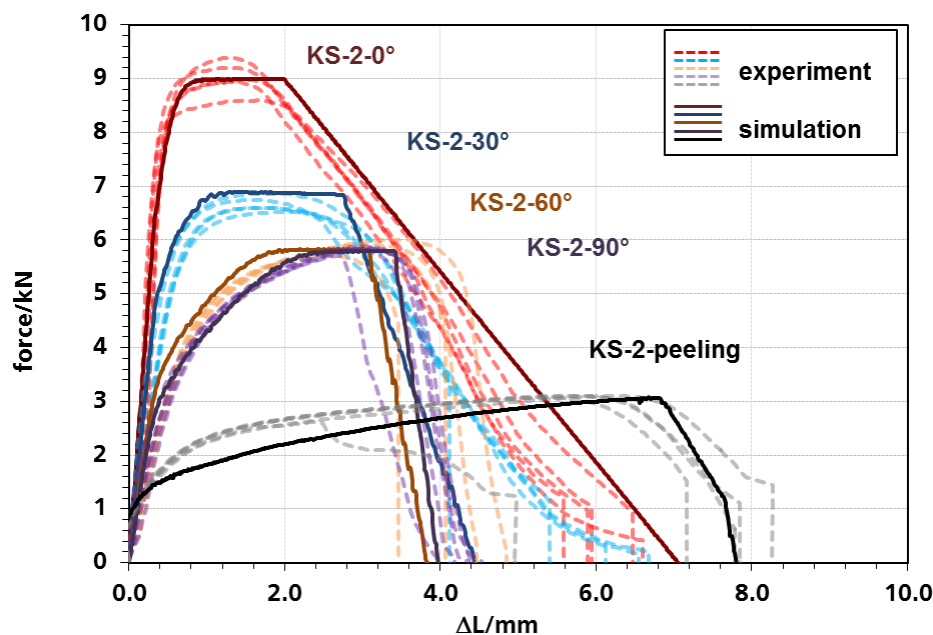

*Fig. 6: Force vs. displacement curves as results of quasi-static simulation of KS-2-0°, 30°, 60°, 90° and peeling test with the *Constrained_SPR3_IWM in comparison with experimental data*

6 Simulation of T-joint experiments

For the validation we examine the T-joint loaded in direction cross the sill with the rivet positions 1 to 9 (see Fig. 8a)). In Fig. 7 the simulation results for the T-joint specimen compared with the experimental data are shown. The global forces match the experimental data. The first force maximum is matched with a small deviation. Thereafter at the same point in time in experiment and simulation the force rapidly decrease. Also after another decrease in force the last plateau is matched well.
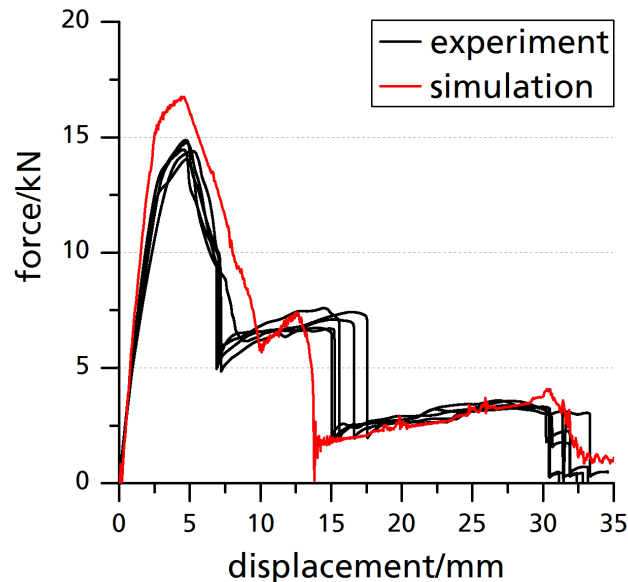
*Fig. 7: Global load in the T-Joint simulation with the *Constrained_SPR3_IWM in comparison with test data*

The deformation behavior of the T-joint specimen caused by the global forces can be represented by the chosen modeling technique in an appropriate quality. The comparison of the deformations between the simulation and the experiment are shown in Fig. 8b. Deviations can be observed in the area of two rivets located in front of the T-joint specimen. In experiment a fold along the connecting line between the both rivets occurs. In contrast the simulation shows almost no deformation in the same area. This discrepancy is partially caused by the modeling method for the sheets in the area of the rivets. In the real specimen a hole in the upper sheet exists which leads to a weak spot and is not considered in the current modeling method.
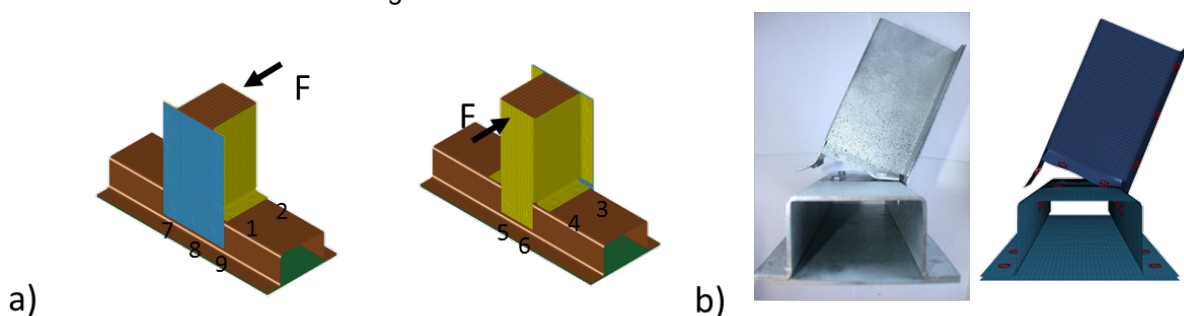

Fig. 8: a) Load directeion and rivet numbering for the T-joint specimen; b) deformation of the T-joint specimen in experiment and simulation under quasistatic load cross the sill

In respect to the rivet failure it is for both simulation and experiment the same. The rivet failure occurs in three steps by pairs. Firstly the two rivets (SPR 5+6) on the front fail. Secondly the two rivets facing the punch on the sides of the T-joint (SPR 2+4) fail. At last the two left rivets (SPR 1+3) fail as well. All these three steps correspond to a decrease of the force in the force vs. displacement curve.
The analysis of the local loading situation (see Fig. 9) of the *Constrained_SPR3_IWM leads to a pure shear load of the rivets 5+6. Hence the shear capacity of the self-piercing riveted joint defines the maximum global force measured in the T-joint loaded in direction cross the sill. For the other rivets the load is a combination of shear and tensile loading. Hence for the shape of the force vs. displacement curve after reaching the maximum force the behavior of the rivet under combined shear and tensile

loading is the crucial factor. Also these joints are not symmetric loaded. So an increased value of sym occurs.
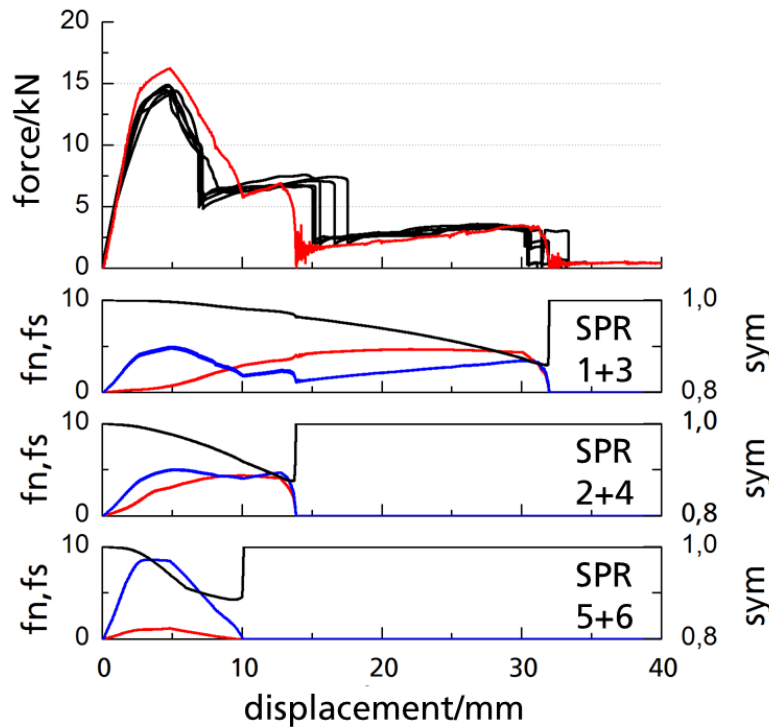

Fig. 9: Global and internal forces of the *Constrained_SPR3_IWM-models in the T-Joint simulation in comparison with test data

The result is a reduction of the transferred force of the *Constrained_SPR3_IWM representing the rivets SPR 1+2+3+4. The value of sym for the rivets SPR 5+6 has no effect caused by the assumed structure of the flow rule, which considers sym only in the term of tensile load. To demonstrate the influence of sym on the global force the values of $\alpha_1, \alpha_2, \alpha_3$ can be set to zero (see Fig. 10). The comparison of simulations with this modified parameter set and the original parameter set, used for the simulation in Fig. 7 ($\alpha_1 \neq 0$; $\alpha_2 \neq 0$; $\alpha_3 \neq 0$), shows a higher force level without considering sym. Also the rivet failure of SPR 1+2+3+4 occurs at higher displacements. So it is necessary to consider sym in the yield and failure behavior to get a better reproduction of the specimen behavior after the first force maximum.
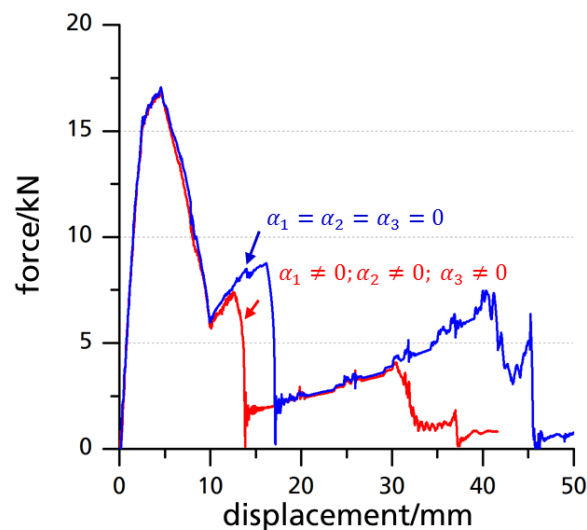

Fig. 10: Influence of a combination of $\alpha_1, \alpha_2, \alpha_3$ and sym on the global force in the T-joint simulation

7 Summary

In this paper a modified approach for the flow and damage behavior of the *Constrained_SPR3 is presented. The modification are described and exemplified. A procedure for the parameter identification is introduced and the application of this procedure is shown for one riveted connection. Using the T-joint specimen the modified model *Constrained_SPR3_IWM is validated for self-piercing riveted connections. The load case for the rivets is identified and the effects of the modified flow and damage behavior are shown. The correlation of the global force vs. displacement curve and the local damage of the rivet joints is demonstrated. Over all we can notice that the *Constrained_SPR3_IWM is a useful modeling technique for self-piercing riveted connections.

8 Acknowledgments

9 Literature

[1]   He, X., Pearson, I.,Young, K.: "Self-pierce riveting for sheet materials: State of the art", Journal of Materials Processing Technology, Volume 199, Issues 1–3, 2008, Pages 27-36

[2]   Seeger, F., Feucht, M., Frank, Th., Keding, B., Haufe, A.: "An Investigation on Spot Weld Modelling for Crash Simulation with LS-DYNA", 4th LS-DYNA Anwenderforum, 2005

[3]   Bier, M., Liebold, C., Haufe, A., Klamser, H.: "Evaluation of a Rate-Dependent, Elasto-Plastic Cohesive Zone Mixed-Mode Consitutive Model for Spot Weld Modeling", 9th LS-DYNA Anwenderforum, 2010

[4]   Marzi, S., Hesebeck, O., Brede, M., Kleiner, F.: "A rate dependet elastoplastic cohseive zone mixed mode model for crash analysis of adhesivly bondes joints", 7th European LS-DYNA Conference, 2009

[5]   Hanssen, A.G., Olovsson, L., Porcaro, R., Langseth, M.: "A large-scale finite element point-connector model for self-piercing rivet connections", European Journal of Mechanics - A/Solids, Volume 29, Issue 4, 2010, Pages 484-495

[6]   LS-DYNA Keyword Users's Manual, Version 971 R6.0.0, Livermore Software Technology Corporation (LSTC), 2012

[7]   Sommer, S., Maier, J.: "Failure Modeling of a self-piercing riveted joint using LS-Dyna", 8th European LS-DYNA Conference, 2011

[8]   Bier, M., Sommer, S.: "Advanced investigations on a simplified modeling method of self-piercing riveted joints for crash simulation", 11th LS-DYNA Anwenderforum, 2012

[9]   Hahn, O., Wissling M., Klokkers, F.: „Ermittlung wahrer Kennwerte für geschraubte und stanzgenietete Blechverbindungen unter schlagartiger Belastung", EFB-Forschungsbericht Nr. 297, 2009